Electronic Supplementary Information

17 March, 2020

Ms. ID: TA-ART-12-2019-013711

Testing the Predictive Power of Theory for $Pd_xIr_{(100-x)}$ Alloy Nanoparticles for the Oxygen Reduction Reaction

Hongyu Guo, Jamie A. Trindell, Hao Li, Desiree Fernandez, Simon M. Humphrey, Graeme Henkelman, Richard M. Crooks

Table of Contents

Table S1. Comparison between the calculated average binding energies (eV) at random alloy (RA) and intermetallic structures. The considered intermetallic structures are shown in **Figure S8.**

	O Binding (RA)	Standard Deviation (RA)	O Binding (Intermetallic)	O Binding Variation	OH Binding (RA)	Standard Deviation (RA)	OH Binding (Intermetallic)	OH Binding Variation
Pd_3	-1.03	0.11	-1.17	0.14	-2.51	0.12	-2.80	0.29
Pd_2Ir_1	-1.59	0.16	-1.45	0.14	-2.91	0.08	-2.88	0.03
Pr_1Ir_2	-1.81	0.15	-2.03	0.22	-2.94	0.07	-2.94	0.00
Ir_3	-1.85	0.11	-2.07	0.22	-2.72	0.24	-2.67	0.05

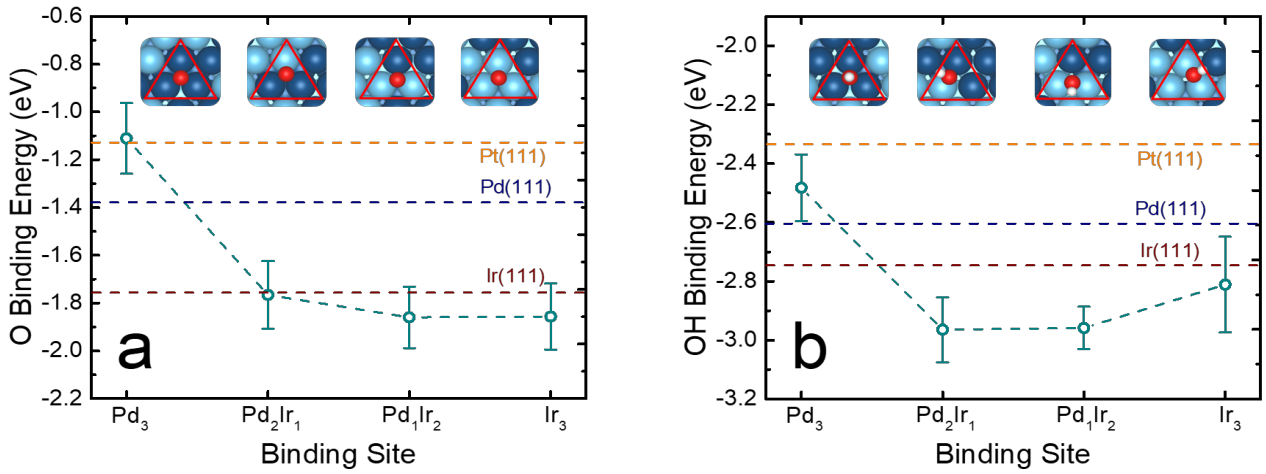

Figure S1. Plots of the calculated (a) O and (b) OH binding energies for the four different triatomic ensembles of PdIr on a randomly alloyed $Pd_{80}Ir_{20}(111)$ model. The red, blue, and orange dashed lines represent the binding energies on Ir(111), Pd(111), and Pt(111), respectively. Each error bar was calculated using ten sampled binding sites on nine randomly alloyed $Pd_{80}Ir_{20}(111)$ surfaces. Insets show the representative optimized binding geometries of O and OH. Blue, light blue, red, and white spheres represent Pd, Ir, O, and H, respectively. Using this alloyed $Pd_{80}Ir_{20}(111)$ model as a supplementary example to compare with the results of $Pd_{50}Ir_{50}(111)$ model in **Figure 1**, we show that different alloy compositions of PdIr do not lead to significant differences in the O and OH binding energies.

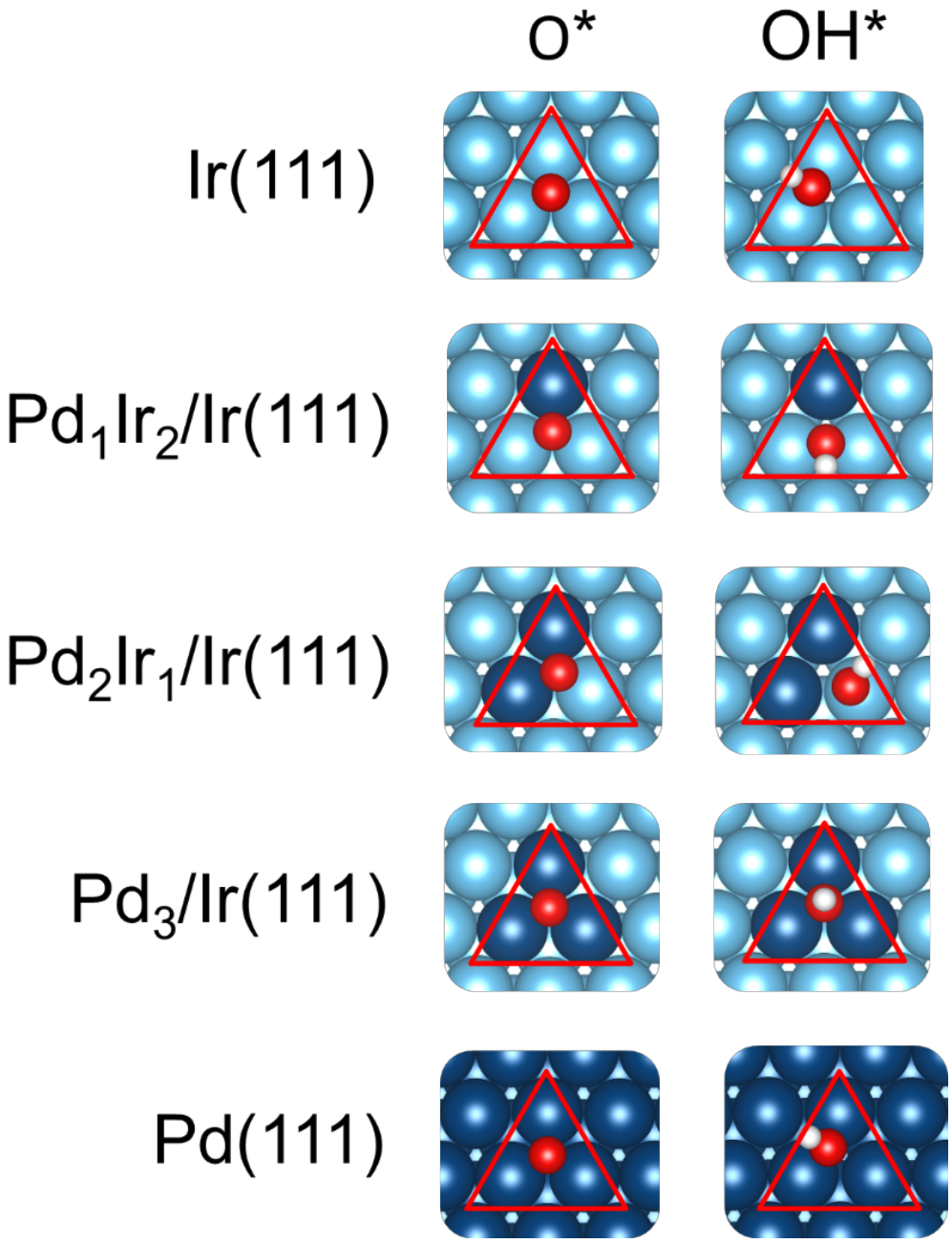

Figure S2. Optimized adsorption configurations of O and OH on Ir(111), Pd_1Ir_2/Ir(111), Pd_2Ir_1/Ir(111), Pd_3/Ir(111), and Pd(111). Dark blue, light blue, red, and white spheres represent Pd, Ir, O, and H, respectively.

Table S2. Calculated average electron charge gain (e) and bond length (Å) of the triatomic ensembles on Ir(111). The charges gain of Ir and Pd was calculated respectively using the electron charge of Ir_3/Ir(111) and Pd_3/Pd(111) as the references.

	Charge Gain (Ir)	Charge Gain (Pd)	Bond Length (Ir-Ir)	Bond Length (Ir-Pd)	Bond Length (Pd-Pd)
Ir(111)	0	N/A	2.73	N/A	N/A
Pd_1Ir_2/Ir(111)	0.05	-0.04	2.74	2.75	N/A
Pd_2Ir_1/Ir(111)	0.06	-0.05	N/A	2.77	2.75
Pd_3/Ir(111)	N/A	-0.01	N/A	N/A	2.78

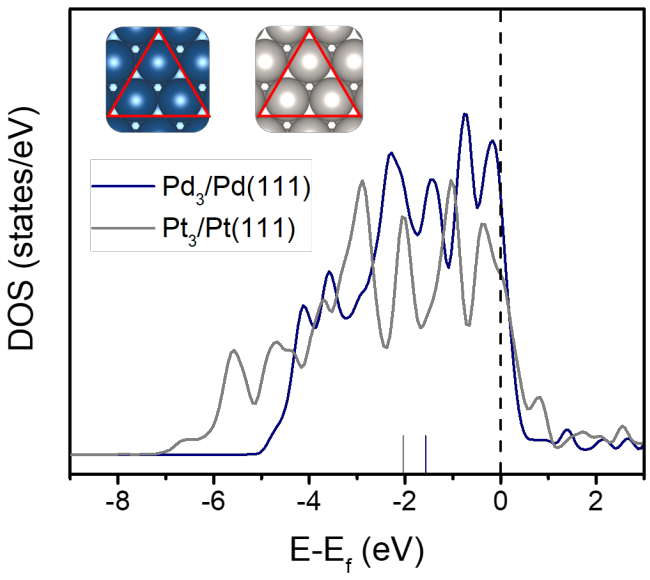

Figure S3. Calculated projected density of states (PDOS) for *d*-electrons of $Pd_3/Pd(111)$ and $Pt_3/Pt(111)$. Insets show the geometries of the triatomic ensembles considered for the calculations. Blue and grey spheres represent Pd and Pt, respectively. The calculated *d*-band center values are -1.58 and -2.06 eV, for $Pd_3/Pd(111)$ and $Pt_3/Pt(111)$, respectively.

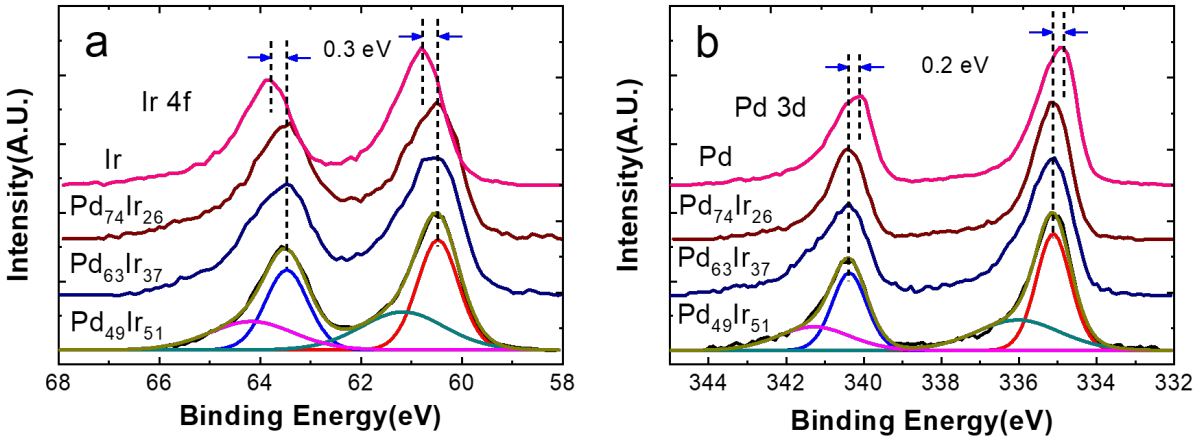

Figure S4. High-resolution XPS spectra for $Pd_xIr_{(100-x)}$ NPs. (a) The Ir 4f region and (b) the Pd 3d region.

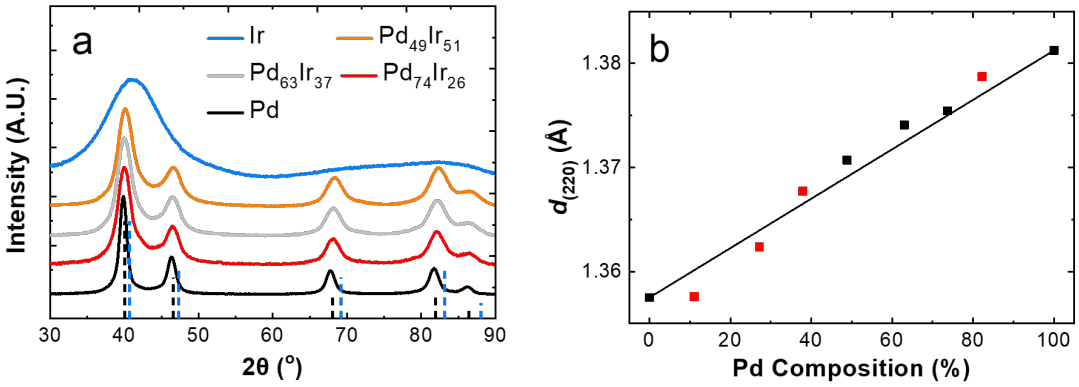

Figure S5. PXRD analysis of $Pd_xIr_{(100-x)}$ NPs. (a) PXRD diffraction patterns of $Pd_xIr_{(100-x)}$ NPs. Standard reference X-ray reflection positions for Pd (JCPDS#004-0802) and Ir (JCPDS#006-0598) are indicated as dashed lines at the bottom of the figure. (b) (220) *d*-spacing values, in Angstroms, as determined from PXRD and plotted as a function of Pd composition from ICP-OES. While in this study we focused on only five different $Pd_xIr_{(100-x)}$ NP compositions (black squares), additional compositions have also been previously synthesized (red squares).

Table S3. Lattice constants for $Pd_xIr_{(100-x)}$ NPs determined via PXRD.

Composition	Lattice parameter (Å)
Pd	3.91
$Pd_{74}Ir_{26}$	3.89
$Pd_{63}Ir_{37}$	3.89
$Pd_{49}Ir_{51}$	3.88

Table S4. Mass-loading (wt%) of each as-synthesized catalyst on Vulcan carbon. The data were determined by ICP-OES prior to any electrochemical treatments.

$Pd_xIr_{(100-x)}$ Catalyst	**Mass-Loading on Vulcan Carbon (wt%)**
Ir/C	2.8%
$Pd_{49}Ir_{51}$/C	1.6%
$Pd_{63}Ir_{37}$/C	1.8%
$Pd_{74}Ir_{26}$/C	2.2%
Pd/C	2.0%

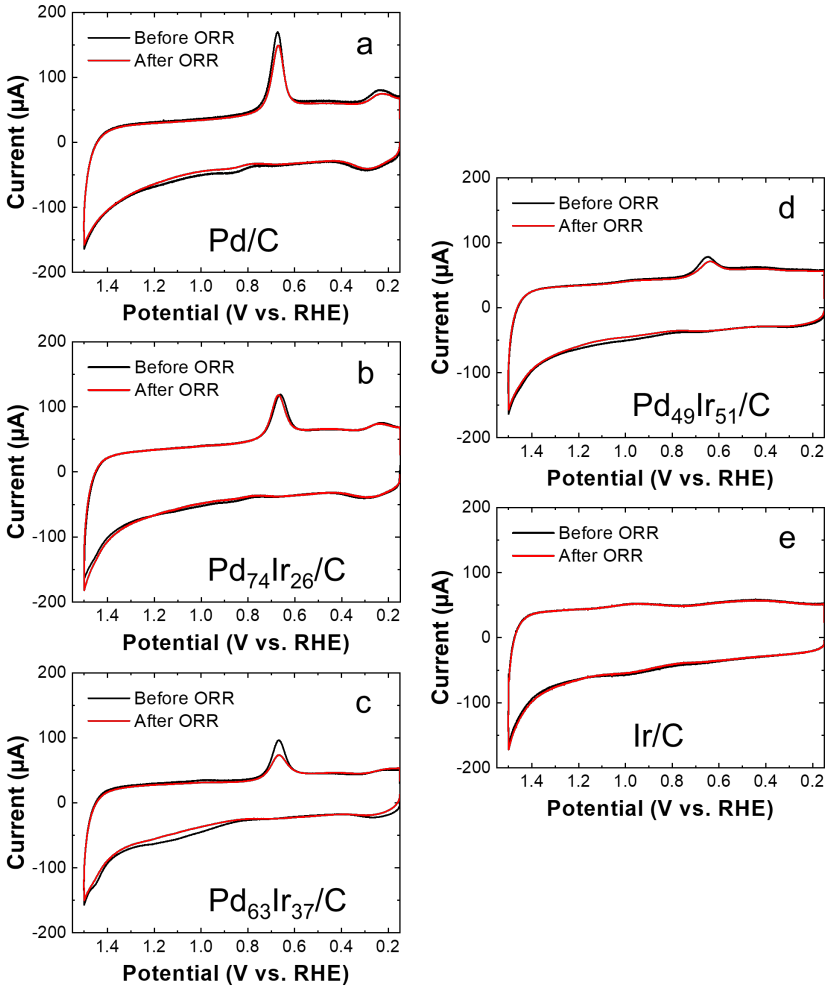

Figure S6. Limiting CVs obtained for $Pd_xIr_{(100-x)}$ NPs before (black trace) and after (red trace) ORR experiments. CVs for (a) Pd/C, (b) $Pd_{74}Ir_{26}/C$, (c) $Pd_{63}Ir_{37}/C$, (d) $Pd_{49}Ir_{51}/C$, and (e) Ir/C were collected in Ar-saturated 0.10 M $HClO_4$ at a scan rate of 50.0 mV/s. The alloy stoichiometries here refer to those determined by ICP-OES for the as-synthesized NPs. To prepare working electrodes, catalyst inks, consisting of the NPs, Vulcan carbon, and Nafion binder were drop cast onto a 3.0 mm glassy carbon disk. The reference electrode was Hg/Hg_2SO_4 (but the potentials have been converted to RHE) and the counter electrode was a glassy carbon rod.

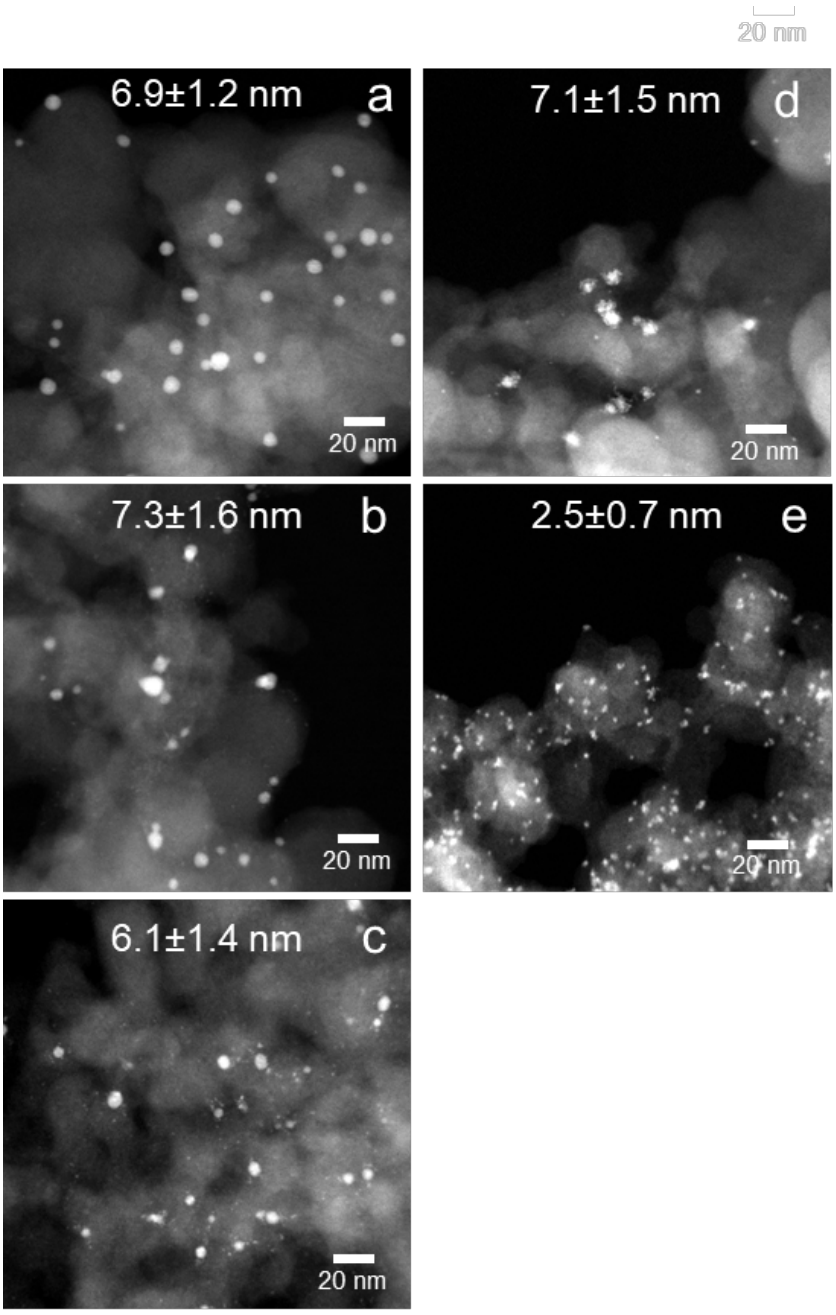

Figure S7. STEM images of the metal NPs used in this study after electrochemical ORR experiments. (a) Pd/C, (b) $Pd_{74}Ir_{26}$/C, (c) $Pd_{63}Ir_{37}$/C, (d) $Pd_{49}Ir_{51}$/C, and (e) Ir/C. The stoichiometries refer to those determined by ICP-OES for the as-synthesized NPs. Size-distributions were obtained by sizing 200 NPs from three individual trials, for a total of 600 NPs analyzed.

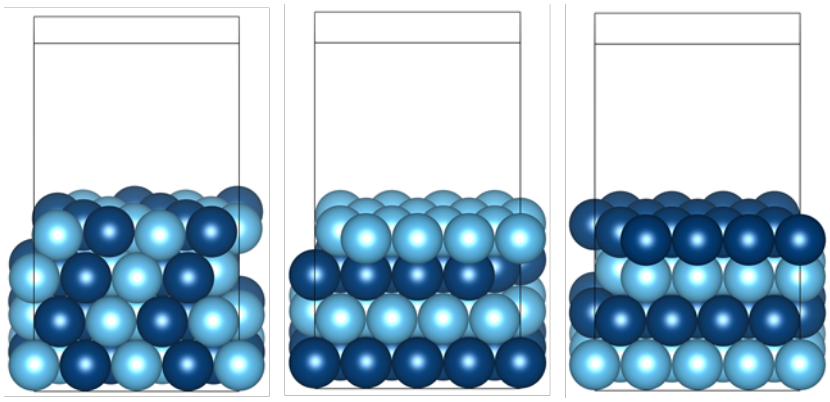

Figure S8. Optimized structures of intermetallic alloy structures. Dark blue and light blue spheres represent Pd and Ir, respectively.